

phant mortalities and that an accurate accounting of this disease has been limited by the unavailability of case material before the 1980s.

The only known survivor of infection by this herpesvirus, Asian elephant case 3, was diagnosed very early in the course of the disease in November 1997 by clinical findings and positive PCR results on peripheral blood. The elephant's clinical recovery in this case was attributed to the use of an anti-herpesvirus drug, famciclovir (14). The favorable drug response shows promise for treatment of future cases of this disease. We are continuing an intensive investigation of these viruses, as we believe the disease they cause represents a threat to elephant conservation. Our findings also have implications for management practices in facilities keeping both African and Asian elephants and in protecting natural elephant habitats from virulent forms of the virus. There is also an urgent need to develop serological tests that can discriminate between the two viruses and permit identification of possible asymptomatic carrier animals.

References and Notes

1. AZA Elephant Species Survival Plan, unpublished statistics (1997).
2. L. K. Richman *et al.*, in preparation.
3. P. Ossent *et al.*, *Vet. Pathol.* **27**, 131 (1990).
4. A. E. Metzler, P. Ossent, F. Gussetti, A. Rubel, E. M. Lang, *J. Wildlife Dis.* **26**, 41 (1990).
5. A. M. Hargis, P. E. Ginn, J. E. K. L. Mansell, R. L. Garber, *Vet. Derm.*, in press.
6. D. R. VanDevanter *et al.*, *J. Clin. Microbiol.* **34**, 1666 (1996).
7. Initially, consensus primer PCR was performed using a published set of redundant primers for the terminase and DNA polymerase gene regions. Specific single primer sets for the elephant herpesvirus terminase and DNA polymerase gene regions were constructed from the sequence initially obtained from elephant cases 1 and 2: terminase primers for Asian elephants (5'-GTACGTCTTCTAGCTCAC-3' and 5'-GTGTCCGCTAAATGTCTTG-3'), terminase primers for African elephants (5'-AATGTGATATCTACGTATG-3' and 5'-GTAATATATCTTATCATGTC-3'), and DNA polymerase primers for both elephant species (5'-GTGTCTGGATAGCAGAGT-3' and 5'-CACATC-GATACGGAATCTCT-3'). PCR amplification was performed with nonredundant primers in a 50- μ l reaction volume containing PCR SuperMix (Gibco/BRL-Life Technologies, Gaithersburg, MD), 0.3% (v/v) glycerol, and 20 pmol of each primer. Thirty-six cycles of PCR were completed using the following protocol: denaturation at 94°C for 1 min, annealing at 50°C for 1 min, and extension at 72°C for 2 min. The final extension was performed at 72°C for 7 min. The PCR product was visualized on a 1.5% agarose gel stained with ethidium bromide. A second round of PCR was needed to detect the African elephant vulval lymphoid patch product using the same terminase primers under identical conditions. Some PCR products were cloned using the TA Cloning kit (Invitrogen) and sequenced, and others were sequenced directly from the PCR products.
8. DNA was extracted from ~100 μ m of paraffin-embedded, formalin-fixed tissue with the Ex-wax kit (Oncor, Gaithersburg, MD). After precipitation, DNA was resuspended and amplified by PCR. DNA was extracted from 200 μ l of whole blood (either fresh or frozen at -80°C) using Genra System (Minneapolis, MN) capture columns according to the manufacturer's protocol.

9. M. C. Persoons, F. S. Stals, M. C. van dam Mieras, C. A. Bruggeman, *J. Pathol.* **184**, 103 (1998).
10. S. Karlin, E. S. Mocarski, G. A. Schachtel, *J. Virol.* **68**, 1886 (1994).
11. E. R. Jacobson, J. P. Sundberg, J. M. Gaskin, G. V. Kollias, M. K. O'Banion, *J. Am. Vet. Med. Assoc.* **189**, 1075 (1986).
12. L. Munson *et al.*, *J. Zoo Wildlife Med.* **26**, 353 (1995).
13. L. Richman, unpublished data.
14. D. L. Schmitt and D. A. Hardy, *J. Elephant Managers Assoc.* **9**, 103 (1998).
15. Funded by NIH grant No. 1 K08 AI01526-01, the Smithsonian Scholarly Studies Program, the Kumari Elephant Conservation Fund, and Friends of the National Zoo. We thank the following individuals and institutions for their contributions to our study: R. Viscidi, Johns Hopkins School of Medicine, for assistance with phylogenetic analysis; J. Strandberg, F. Hamzeh, and A. Shahkolahi, Johns Hopkins School of Medicine; J. Cohen, NIH; S. Feldman, Anmed/Biosafe Inc.; S. Mikota, Audubon Institute; R. Mirkovic, Southwest Foundation for Biomedical Research; J. d'Offay and R. Eberle, Oklahoma State University; G. Letchworth, University of Wisconsin-Madison; K. E. Steele,

B. Connolly, and P. Jahrling, U.S. Army Medical Research Institute of Infectious Diseases; A. Ruebel, Zoo Zürich; P. Ossent, University of Zürich; F. Osorio, University of Nebraska, Lincoln; S. Kania, University of Tennessee, Knoxville; E. Dierenfeld, New York Wildlife Conservation Society; J. Trupkiewicz, L. Munson, and D. Taylor, University of California, Davis; D. Nichols, N. Spangler, K. Clark, J. Sutton, N. Pratt, J. Block, M. Bush, and the elephant keeper staff, National Zoological Park; J. Jenkins and R. V. Ferris, Armed Forces Institute of Pathology; J. Gaskin, University of Florida; D. Olson, African elephant Species Survival Plan (SSP) coordinator; M. Keele, Asian elephant SSP coordinator; A. Schanberger, Houston Zoological Gardens; Marine World Africa-USA, Vallejo, CA; L. Bingaman-Lackey, AZA; N. Kriek, University of Pretoria, South Africa; R. Bengis, Kruger National Park, South Africa; and San Diego Zoo and Wild Animal Park, New York Wildlife Conservation Society, Lincoln Park Zoo, Dickerson Park Zoo, African Lion Safari, Tulsa Zoological Park, Fort Worth Zoo, Indianapolis Zoo, Dallas Zoo, Oakland Zoo, and the Center for Reproduction of Endangered Species.

2 October 1998; accepted 19 January 1999

Three-Dimensional Structure of a Recombinant Gap Junction Membrane Channel

Vinzenz M. Unger,^{1*} Nalin M. Kumar,¹ Norton B. Gilula,¹ Mark Yeager^{1,2†}

Gap junction membrane channels mediate electrical and metabolic coupling between adjacent cells. The structure of a recombinant cardiac gap junction channel was determined by electron crystallography at resolutions of 7.5 angstroms in the membrane plane and 21 angstroms in the vertical direction. The dodecameric channel was formed by the end-to-end docking of two hexamers, each of which displayed 24 rods of density in the membrane interior, which is consistent with an α -helical conformation for the four transmembrane domains of each connexin subunit. The transmembrane α -helical rods contrasted with the double-layered appearance of the extracellular domains. Although not indicative for a particular type of secondary structure, the protein density that formed the extracellular vestibule provided a tight seal to exclude the exchange of substances with the extracellular milieu.

Gap junction membrane channels are macromolecular complexes that allow the direct exchange of small molecules and ions between neighboring cells (1); thus, these channels have an important role in maintaining homeostasis within tissues. Electrophysiological measurements, as well as dye-transfer studies *in vivo*, have revealed that signal transmission through gap junctions can be modulated by a variety of molecules and physiologic conditions [reviewed in (2-5)].

A diverse multigene family of polytopic gap

junction membrane proteins are known as connexins (5, 6). Several human diseases have been related to connexin mutations, such as the X chromosome-linked form of Charcot-Marie-Tooth disease (7, 8); the most common form of nonsyndromic neurosensory autosomal recessive deafness (9, 10); and, possibly, developmental anomalies of the cardiovascular system in some patients (11). In addition, transgenic mice lacking α_1 connexin43, the principal gap junction protein in the heart, die soon after birth and exhibit developmental malformations (12, 13). Heterozygotes are viable but display slowed ventricular conduction (14).

Previous analyses of gap junction structure have been limited to relatively low resolution, which is partially due to the heterogeneity of the specimens (15). A model based on electron microscopy and x-ray-scattering experiments suggests that the intercellular channel is formed by the end-to-end interaction of two oligomers

¹The Scripps Research Institute, Department of Cell Biology, 10550 North Torrey Pines Road, ²Division of Cardiovascular Diseases, Scripps Clinic, 10666 North Torrey Pines Road, La Jolla, CA 92037, USA.

*Present address: Max-Planck-Institut für Biophysik, Abteilung Strukturbiologie, Heinrich-Hoffmann-Strasse 7, D-60528 Frankfurt am Main, Germany.

†To whom correspondence should be addressed. E-mail: yeager@scripps.edu

REPORTS

termed connexons (16, 17). Within these oligomers, each connexin subunit is thought to traverse the membrane bilayer four times, placing the NH₂- and COOH-termini on the cytoplasmic membrane surface [(18–20) and reviewed in (15)].

A major challenge in the structure analysis of low-abundance polytopic integral membrane proteins has been the development of systems that enable the overexpression of sufficient functional material. We have generated stably transfected baby hamster kidney (BHK) cell lines that can be induced to express wild-type and mutant connexins (21, 22). A mutant of α_1 connexin that lacks most of the COOH-terminal domain (α_1 -Cx263T) assembles into bona fide gap junctions. Although the level of expression is quite low in comparison with the expression of soluble proteins in bacterial systems, the structure analysis has nevertheless been feasible with just microgram amounts of recombinant material. A projection density map, which was derived by electron crystallography of frozen and hydrated two-dimensional (2D) crystals of the recombinant gap junctions, reveals a ring of transmembrane α helices that lines the aqueous pore and a second ring of α helices that is in close contact with the membrane lipids (22). To further explore the transmembrane architecture of the channel, we extended the analysis into the third dimension by recording and analyzing low-dose images of frozen and hydrated, tilted 2D crystals that had been treated with oleamide

(23–25). The resulting three-dimensional (3D) density map was determined at resolutions of ~ 7.5 Å in the membrane plane and 21 Å in the vertical direction (Fig. 1 and Table 1).

A side view of the 3D map (Fig. 2) showed that the recombinant gap junction channel formed by the α_1 -Cx263T mutant had a thickness of ~ 150 Å when the map was contoured at 1.5σ . This reduced thickness, in comparison with ~ 250 Å for native cardiac gap junction channels (15), was consistent with the lack of the 13-kD cytoplasmic COOH-tail in α_1 -Cx263T. The outer boundary of the map revealed a tripartite arrangement that consisted of two membrane domains that were separated by an extracellular domain. The outer diameter within the membrane region was ~ 70 Å, and there was a pronounced waist in the extracellular portion of the channel where the outer diameter decreased abruptly by ~ 20 Å. However, the external contours of the channel did not correlate with the shape of the aqueous pathway. A vertically sectioned view of the map (Fig. 2b) revealed that the channel narrowed from ~ 40 to ~ 15 Å (neglecting the contributions of amino acid side chains) in proceeding from the cytoplasmic to the extracellular side of the bilayer. The aqueous pathway then widened again to a diameter of ~ 25 Å within the extracellular vestibule.

Elements of secondary structure were revealed more clearly by the examination of cross sections that are parallel with the planes

of the membranes (Fig. 2c). In particular, sections within the hydrophobic region of the bilayers (Fig. 2c, top and bottom) displayed roughly circular contours of density that were typical, at the current limit of resolution, for cross sections of α helices. Because there were 24 circular densities per hexameric connexon, we conclude that the dodecameric channel contains 48 transmem-

Table 1. Data analysis summary.

Parameter	Value
Number of images	69
Unit cell parameters	$a = b = 76.8$ Å $\gamma = 120^\circ$
Two-sided plane group	p6
Range of crystal tilts	0° to 35.3°
Range of underfocus	-2000 to $-15,000$ Å
Total number of measurements*	8256
Total number of fitted unique reflections†	1022
Overall weighted phase error‡	18.9°
Effective resolution cutoffs§	7.5 Å (in plane) 21.0 Å (vertical)

*For all observations, 62% had a signal-to-noise ratio of at least 2.3 (IQ3 or better). †Out of 1258 unique reflections expected at an in-plane resolution of up to 7.5 Å and a maximum tilt of 35°. At 30° tilt, a total of 1088 reflections are expected, and the data effectively sample >90% of reciprocal space for this lower tilt value. ‡For the fit of lattice lines, including all data to IQ8 to a nominal in-plane resolution of 7.5 Å. §Measured from the point-spread function of the fitted data set (44).

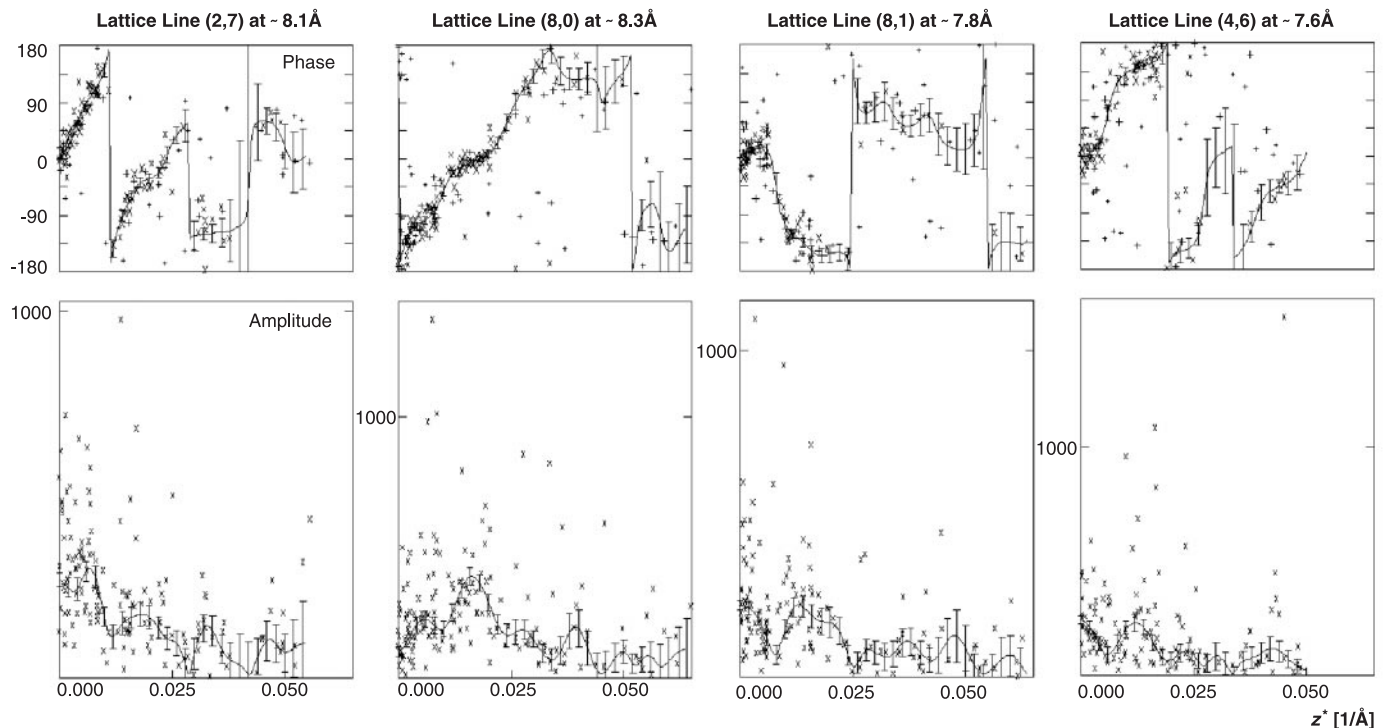


Fig. 1. Amplitude and phase variations along higher resolution lattice lines after merging data from tilted crystals in the two-sided plane group p6. The points include all data with a signal-to-noise ratio of >1 (IQ8 and better). The continuous curves were computed by the program LATLINE (41). The horizontal z^* axis is the distance from the origin of the lattice

line. Symbols in the phase plots refer to the quality of the data, as given by IQ values (37) (X, IQ values of 1 and 2; x, IQ values of 3 and 4; large +, IQ values of 5 and 6; small +, IQ values of 7 and 8). Data with IQ1 and IQ7 correspond to signal-to-noise ratios of 8 and 1, respectively. Error bars, SD of phases and amplitudes for the fitted structure factor.

brane α helices. Thus, the widely accepted topological model in which each connexin subunit has four transmembrane α helices was confirmed.

A view along the channel axis (Fig. 3a) provided a more detailed description for the packing arrangement of the transmembrane α helices. Four of the α helices were arbitrarily labeled A, B, C, and D for reference. As was suggested by our previous projection density map (22), the α helix in position A and its symmetry-related equivalents were oriented almost perpendicular to the membrane plane. The B α helix was almost parallel to the A α helix through the hydrophobic core of the membrane. However, this was not resolved in projection because of the additional contribution of the highly structured extracellular domains. The packing of the α helices can be seen particularly well in Fig. 3b, which displays an enlarged view of α helices C, D, A', and B'. The sets of α -helical pairs C/D, D/A', A'/B', and B'/C all packed with a left-handed twist. However, the channel-lining B/C pair packed with a right-handed twist. The predominantly left-handed packing of the α helices within the connexon contrasts with the right-handed α -helical barrel observed for the aquaporin-1 monomer (26–28). The right-handed packing of the B/C pair of α helices was similar to the right-handed packing of the α helices that line the putative

ion pathway in the H^+ (29) and Ca^{2+} adenosine triphosphatases (30), which also showed mixed left- and right-handed α -helical packing within the bundle.

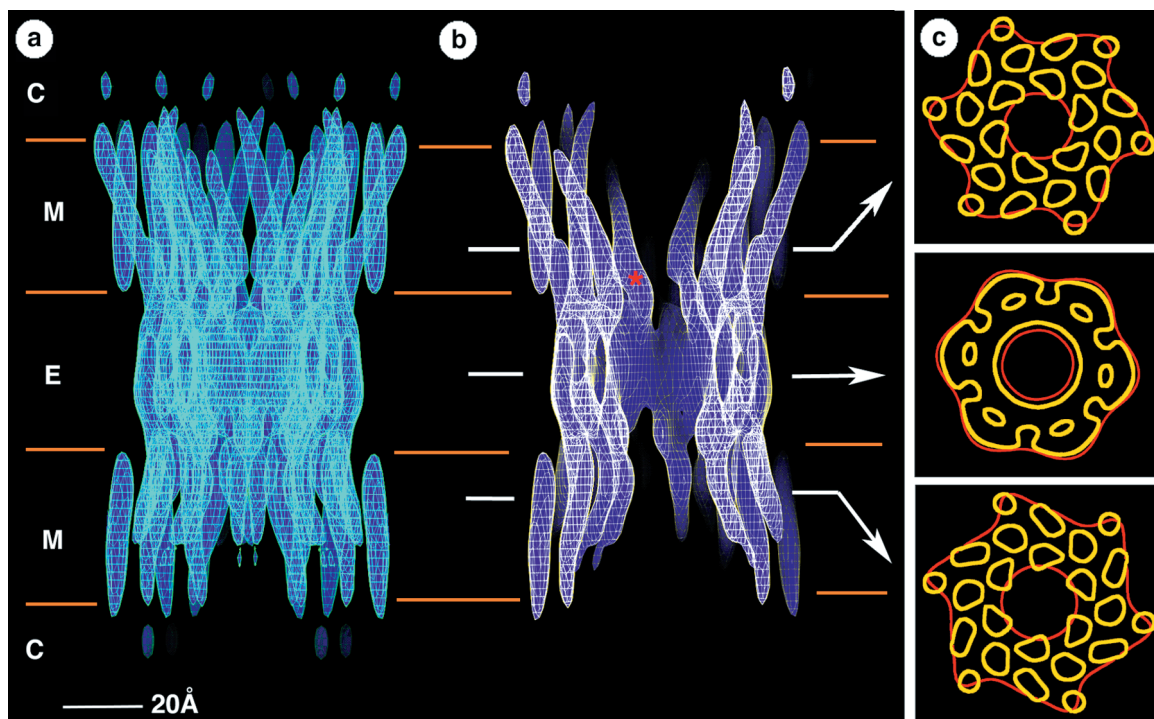
The tilt of the channel-lining C α helix accounted for the narrowing of the pore from ~ 40 to ~ 15 Å at the boundary with the extracellular gap. These approximate dimensions did not account for amino acid side chains, which are not visualized at a resolution of 7.5 Å. If the amino acid side chains were considered, then the narrowest constriction of the pore would be ~ 5 Å in diameter. However, at present, it would be premature to correlate the observed dimensions of the pore with a specific conformational state.

The substantial tilt of the C α helix was unexpected because it appeared to be oriented almost perpendicular to the membrane plane in projection (22). The 3D map revealed that the part of this α helix that was observed in projection was located toward the boundary with the extracellular gap where a bend in the density shifted the α helix to an orientation that was nearly perpendicular to the membrane plane before merging with the continuous wall of density that constituted part of the extracellular domain (Figs. 2b and 3b). The angled portion of the C α helix within the membrane interior extended over the central band of density at a radius of 25 Å and therefore was not resolved in

the projection map. The substantial tilt of the C α helix exposed parts of the B α helix to the pore so that two α helices contributed to the lining of the pore.

One would expect a priori that the interior of the channel necessarily has to be separated from the lipid regions by protein. With this assumption, the length of the A α helix was shortest and was thus likely to demarcate the approximate vertical boundaries of the lipid bilayer. Hence, the continuation of the B and C α helices beyond the visible end of the A α helix (that is, toward the observer in Fig. 3a) represented polypeptides in the cytoplasmic region (for example, the NH_2 -tail, residual $COOH$ -tail in the mutant, or residues in the M2-M3 loop connecting the second and third transmembrane α helices). These extensions had a rodlike morphology that was similar to their transmembrane counterparts, suggesting that cytoplasmic portions of the molecule were not only well ordered but also adopted an α -helical structure. However, this well-ordered density could not be unambiguously ascribed to particular regions of the protein sequence. Nevertheless, the map did reveal distinctive spatial relations for the α helices. For instance, the extension of the B α helix sloped away from the A α helix (that is, clockwise in Fig. 3a), which may have indicated that there is no direct connectivity between these α helices on the cytoplasmic side of the

Fig. 2. Molecular organization of a recombinant gap junction channel. (a) A full side view is shown, and (b) the density has been cropped to show the channel interior. The approximate boundaries for the membrane bilayers (M), extracellular gap (E), and the cytoplasmic space (C) are indicated. The white arrows identify the locations of (c) the cross sections that are parallel to the membrane bilayers. The red contours in (c) are at 1σ above the mean density and include data to a resolution of 15 Å. These contours define the boundary of the connexon and can be compared to previous low-resolution structural studies of liver (16, 17) and heart (20) gap junctions. The yellow contours at 1.5σ above the mean density include data to a resolution of 7.5 Å. The roughly circular shape of these contours within the hydrophobic region of the bilayers is consistent with 24 transmembrane α helices per connexon. The maps in (a) and (b) were contoured at 3σ above the mean, which tends to eliminate density that is less well defined, such as the cytoplasmic domains visualized in Fig. 3a, which are contoured at 1.5σ above



the mean. The red asterisk in (b) marks the narrowest part of the channel where the aqueous pore is ~ 15 Å in diameter, not accounting for the contribution of amino acid side chains that are not resolved at the current limit of resolution. The noncrystallographic twofold symmetry that relates the two connexons of a gap junction channel has not been applied to the map. Hence, the similarity of the two connexons provides an independent measure of the quality of this reconstruction.

REPORTS

membrane. The C α helix had a trajectory that extended counterclockwise toward the B α helix, allowing the C α helix to pass between the B and D α helices. This arrangement of the B, C, and D α helices enabled close interactions of at least two of the three cytoplasmic domains (NH₂-tail, COOH-tail, and M2-M3 loop). Given the clustering of charged residues in these domains, the interactions may be stabilized by salt bridges.

Docking between connexons involves interactions between the extracellular loops, which display the most similarity in sequence between connexins but still influence the selectivity of docking between different connexons across the extracellular gap (31, 32). The extracellular region of the 3D structure appeared double layered with a continuous band of density at a radius of ~ 17 Å and six arcs of density at a radius of ~ 26 Å (Fig. 2c, middle). The extracellular density was in distinct contrast to the characteristic "signature" for α helices in cross section (Fig. 2c, top and bottom). This difference implied that at least a portion of the polypeptide within the extracellular gap did not adopt an α -helical conformation. In fact, site-directed mutagenesis has been used by others to shift four of the six conserved cysteines in the extracellular loops of β_1 connexin32 individually, in all possible pairwise combinations, and even in some quadruple combinations (33). Foote *et al.* used the pattern of periodicity for the cysteine positions that produced functional channels to suggest a model in which the extracellular loops fold as antiparallel β sheets (33). Although the precise secondary structure within the gap was not revealed in our 3D map, it was nevertheless clear that the interior band of density provided a continuous wall of protein (Fig. 2b), which functions as a tight electrical

and chemical seal to exclude the exchange of substances with the extracellular milieu.

Because the connecting loops between the transmembrane α helices were not revealed in our map at an in-plane resolution of 7.5 Å, there was ambiguity in assigning the molecular boundary of the connexin subunit. However,

there were only a small number of reasonable subunit boundaries. Each of the three possible models shown in Fig. 4 predicted different molecular contacts at the subunit interfaces. It seemed likely that each of these arrangements could involve different mechanisms for the oligomerization of subunits during the assembly

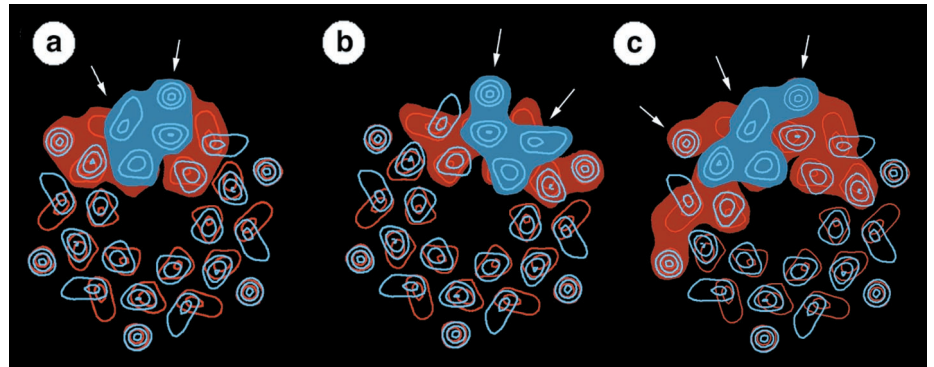
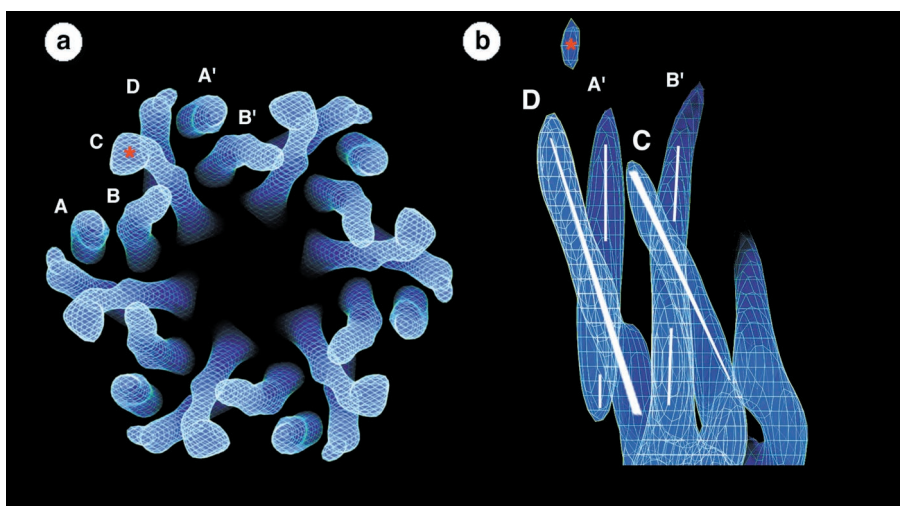


Fig. 4. Superposition of cross sections (red and blue) within the hydrophobic region of the two hexameric connexons forming the gap junction channel. The shaded regions identify three possible boundaries for the connexin subunit. With reference to the labels in Fig. 3a, the models show (a) a bundle of four α helices (A'DCB'), (b) a check-mark arrangement (ABCD), and (c) a zigzag pattern (BCDA'). White arrows identify axes of symmetry that are in plane, noncrystallographic, and twofold. In (a) and (b), the blue subunit of one connexon overlaps two red subunits in the apposing connexon. The α helices within each subunit are aligned along only two of the local twofold axes of symmetry, and consequently, the centers of gravity for subunits in the apposed connexons are not in register. Such an arrangement can only be realized if the apposed connexons dock with a 30° rotational stagger across the extracellular gap. These models are consistent with our interpretation of the projection density map (22) and with a recent analysis at a resolution of ~ 18 Å of negatively stained gap junction plaques that had been split in the extracellular gap by urea treatment (42). Six protrusions of density on the extracellular surface of the connexon could only be docked to form a tight seal if these protrusions interdigitated with a 30° stagger (43). However, the model in (c) demonstrates that not all possible subunit boundaries involve rotational stagger between the apposed connexons. In (c), each blue subunit of one connexon overlaps three red subunits in the apposed connexon, and the four α helices of a putative subunit would be associated with three of the local twofold axes of symmetry. The centers of gravity of the subunits in the two connexons would be superimposed, and hence the connexons would dock in register. Noncrystallographic twofold symmetry between the two connexons was not imposed. The almost perfectly preserved twofold symmetry in the superimposed red and blue density contours provides an independent check of the quality of the reconstruction.

Fig. 3. (a) A top view looking toward the extracellular gap and (b) a side view of part of the 3D map of a recombinant gap junction channel. For clarity, only the cytoplasmic and most of the membrane-spanning regions of one connexon are shown. The 24 well-resolved rod-shaped features reveal the packing of the transmembrane α helices, and four have been arbitrarily labeled A, B, C, and D as points of reference for discussion. Similarly, A' and B' identify putative α helices that are identical to A and B because of the sixfold symmetry of the channel. Within the hydrophobic core of the membrane (see Fig. 2c, top and bottom), it would appear that the favored molecular boundary is the four-helix bundle, as shown in (b) (see also Fig. 4a). However, toward the cytoplasmic surface, the α helices spread apart such that the interactions appear to favor the "check-mark" model ABCD in (a) (see also Fig. 4b). The view in (a) was contoured at 1.5 σ above the mean density, and the view in (b) was contoured at 3 σ above the mean density to avoid obstructing the A' α helix by the continuation of density that extends the C α helix into the cytoplasmic space. The red asterisk in (a) marks the density that is closest to the observer and indicates that the C α helix extends well beyond the putative boundary of the bilayer on the cytoplasmic face. The equivalent position is indicated by the red asterisk in (b). White lines in (b) follow the center of gravity for the four α helices and also indicate the direction of helix tilt. The wider ends of the lines for the C and D α helices are closer to the observer (that is, from top to bottom, the C α helix slopes away from the observer, whereas the D α helix slopes toward the observer).



of the intercellular channel. Definition of the specific molecular boundary will require at least an unambiguous assignment of the transmembrane α helices to the four hydrophobic domains in the amino acid sequence. Nevertheless, these three models emphasized that connexon docking involves multivalent interactions of subunits between connexons, which would confer stability in the formation of the intercellular channel and may in part be required for achieving selectivity in the docking process.

References and Notes

1. W. R. Loewenstein, *Physiol. Rev.* **61**, 829 (1981).
2. F. Ramón and A. Rivera, *Prog. Biophys. Mol. Biol.* **48**, 127 (1986).
3. D. C. Spray and J. M. Burt, *Am. J. Physiol.* **258**, C195 (1990).
4. E. C. Beyer and R. D. Veenstra, in *Handbook of Membrane Channels*, C. Peracchia, Ed. (Academic Press, San Diego, CA, 1994), pp. 379–401.
5. R. Bruzzone, T. W. White, D. L. Paul, *Eur. J. Biochem.* **238**, 1 (1996).
6. N. M. Kumar and N. B. Gilula, *Cell* **84**, 381 (1996).
7. J. Bergoffen et al., *Science* **262**, 2039 (1993).
8. L. J. Bone et al., *Neurobiol. Dis.* **4**, 221 (1997).
9. L. Zelante et al., *Hum. Mol. Genet.* **6**, 1605 (1997).
10. T. W. White, M. R. Deans, D. P. Kelsell, D. L. Paul, *Nature* **394**, 630 (1998).
11. S. H. Britz-Cunningham, M. M. Shah, C. W. Zuppan, W. H. Fletcher, *N. Engl. J. Med.* **332**, 1323 (1995).
12. A. G. Reaume et al., *Science* **267**, 1831 (1995).
13. J. L. Ewart et al., *Development* **124**, 1281 (1997).
14. P. A. Guerrero et al., *J. Clin. Invest.* **99**, 1991 (1997).
15. M. Yeager, *J. Struct. Biol.* **121**, 231 (1998).
16. P. N. T. Unwin and P. D. Ennis, *Nature* **307**, 609 (1984).
17. L. Makowski, D. L. D. Caspar, W. C. Phillips, D. A. Goodenough, *J. Cell Biol.* **74**, 629 (1977).
18. L. C. Milks et al., *EMBO J.* **7**, 2967 (1988).
19. S. B. Yancey et al., *J. Cell Biol.* **108**, 2241 (1989).
20. M. Yeager and N. B. Gilula, *J. Mol. Biol.* **223**, 929 (1992).
21. N. M. Kumar, D. S. Friend, N. B. Gilula, *J. Cell Sci.* **108**, 3725 (1995).
22. V. M. Unger, N. M. Kumar, N. B. Gilula, M. Yeager, *Nature Struct. Biol.* **4**, 39 (1997).
23. Expression and 2D crystallization of α_1 -Cx263T was performed as described in (22), with the following modifications. The sleep-inducing lipid oleamide (34), which has been shown to induce gap junction closure in vivo (35), and the trifluoromethylketone inhibitor of fatty acid amide hydrolase (36) were present during the induction period of the BHK cells at concentrations of 100 and 1 μ M, respectively. Oleamide was added in an attempt to investigate if it caused conformational changes in comparison to our previous projection map. The addition of the inhibitor was necessary because BHK cells showed an oleamide-hydrolyzing enzymatic activity. Because the in vivo effects of the oleamide are reversible, this lipid was also added during all stages of the specimen preparation (100 μ M), the detergent extraction of the membranes (200 μ M), and the final dialysis (100 μ M) of the sample. Stock solutions of oleamide and the trifluoromethylketone inhibitor were prepared in ethanol and added to the growth medium just before use. The final ethanol concentration in the medium was 0.1%.
24. Carbon-coated molybdenum grids and frozen and hydrated specimens were prepared as previously described (22). Low-dose electron micrographs of specimens tilted from 0° to 35° were recorded on a Philips CM200FEG microscope at an accelerating voltage of 200 kV, a nominal magnification of 50,000, and defocus values ranging from -2000 to -15,000 Å. Crystal quality was assessed by the optical diffraction of electron micrographs, and only those images with spots visible to a resolution of at least 11 Å were selected for further processing. Micrographs were digitized on a Perkin-Elmer flatbed microdensitometer at a 10- μ m step size

- (corresponding to 2 Å sampling at the level of the specimen). The MRC image-processing package, which was developed by R. Henderson and colleagues (37–39), was used to analyze the images and to correct for lattice distortions and effects of the contrast transfer function. Initial estimates for the tilt parameter of each crystal were obtained from the changes of the contrast transfer function across the image. Image data were then merged in plane group p6, and lattice lines were fitted with a real-space envelope of 220 Å. Considering only data to a resolution of 15 Å, we refined the tilt geometries of the crystals against a raw 3D model before refining the underfocus values of all images to a resolution of ~7 Å. All images were then processed a second time with back projections of the refined 3D model for the cross-correlation search [R. Henderson, program: MAKETRAN (unpublished program)]. This gave a better description of the lattice distortions and, consequently, a more accurate correction of the image. The improved raw data were subjected to two more cycles of tilt geometry and underfocus refinements, and individual resolution cutoffs were determined for each image before the final merging of data. Density maps were calculated with and without imposing an inverse *B* factor to ensure that the enhancement of the weak image-derived amplitudes at higher resolution did not introduce spurious density outside the low-resolution molecular boundary. An inverse temperature factor of *B* = -350 was found to be adequate. Application of this sharpening increased the amplitudes at 7.5 Å by a factor of 4.7. The 3D density map was visualized with the program O (40).
25. M. Yeager, V. M. Unger, A. K. Mitra, *Methods Enzymol.* **294**, 135 (1999).
26. A. Cheng et al., *Nature* **387**, 627 (1997).
27. H. Li, S. Lee, B. K. Jap, *Nature Struct. Biol.* **4**, 263 (1997).
28. T. Walz et al., *Nature* **387**, 624 (1997).
29. M. Auer, G. A. Scarborough, W. Kühlbrandt, *ibid.* **392**, 840 (1998).
30. P. Zhang et al., *ibid.*, p. 835.
31. C. Elfgang et al., *J. Cell Biol.* **129**, 805 (1995).
32. T. W. White, D. L. Paul, D. A. Goodenough, R. Bruzzone, *Mol. Biol. Cell* **6**, 459 (1995).
33. C. I. Foote, L. Zhou, X. Zhu, B. J. Nicholson, *J. Cell Biol.* **140**, 1187 (1998).
34. B. F. Cravatt et al., *Science* **268**, 1506 (1995).
35. X. Guan et al., *J. Cell Biol.* **139**, 1785 (1997).
36. B. F. Cravatt et al., *Nature* **384**, 83 (1996).
37. R. Henderson et al., *Ultramicroscopy* **19**, 147 (1986).
38. R. Henderson et al., *J. Mol. Biol.* **213**, 899 (1990).
39. R. A. Crowther, R. Henderson, J. M. Smith, *J. Struct. Biol.* **116**, 9 (1996).
40. T. A. Jones, J.-Y. Zou, S. W. Cowan, M. Kjeldgaard, *Acta Crystallogr.* **A47**, 110 (1991).
41. D. A. Agard, *J. Mol. Biol.* **167**, 849 (1983).
42. G. Perkins, D. Goodenough, G. Sosinsky, *Biophys. J.* **72**, 533 (1997).
43. ———, *J. Mol. Biol.* **277**, 171 (1998).
44. V. M. Unger and G. F. Schertler, *Biophys. J.* **68**, 1776 (1995).
45. We gratefully acknowledge the technical assistance of D. W. Entrikin. This work has been supported by grants from NIH (M.Y. and N.B.G.), the Lucille P. Markey Charitable Trust (N.B.G.), the Gustavus and Louise Pfeiffer Research Foundation (M.Y.), and the Baxter Research Foundation (M.Y.). V.M.U. was a recipient of a postdoctoral fellowship from the American Heart Association. During the course of this work, M.Y. was an Established Investigator of the American Heart Association and Bristol-Myers Squibb and is now the recipient of a Clinical Scientist Award in Translational Research from the Burroughs Wellcome Fund.

29 September 1998; accepted 4 January 1999

Regulation of Neurotrophin-3 Expression by Epithelial-Mesenchymal Interactions: The Role of Wnt Factors

Ardem Patapoutian,^{1*} Carey Backus,² Andreas Kispert,³ Louis F. Reichardt^{1,2}

Neurotrophins regulate survival, axonal growth, and target innervation of sensory and other neurons. Neurotrophin-3 (NT-3) is expressed specifically in cells adjacent to extending axons of dorsal root ganglia neurons, and its absence results in loss of most of these neurons before their axons reach their targets. However, axons are not required for NT-3 expression in limbs; instead, local signals from ectoderm induce NT-3 expression in adjacent mesenchyme. Wnt factors expressed in limb ectoderm induce NT-3 in the underlying mesenchyme. Thus, epithelial-mesenchymal interactions mediated by Wnt factors control NT-3 expression and may regulate axonal growth and guidance.

Neurotrophins are a family of proteins expressed in target tissues that regulate neuronal survival, differentiation, and function (1).

These trophic factors mainly signal through the Trk family of receptor tyrosine kinases that are found on neuronal cell bodies and projections. Gene-targeting experiments have shown that neurotrophins and Trk receptors are required for survival of specific neuronal populations within the peripheral nervous system (1). NT-3 is essential for the survival of most sensory neurons early in development before they reach their final target, at which point they may gain access to target-

¹Department of Physiology, ²Howard Hughes Medical Institute, University of California, San Francisco, CA 94143–0723, USA. ³Department of Molecular Embryology, Max-Planck-Institute for Immunobiology, Stuebeweg 51, D-79108 Freiburg, Germany.

*To whom correspondence should be addressed. E-mail: ardem@itsa.ucsf.edu